Substituent Effects on Energetics and Crystal Morphology Modulate Singlet Fission in 9,10-Bis(phenylethynyl)anthracenes

Youn Jue Bae, Joseph A. Christensen, Gyeongwon Kang, Jiawang Zhou, Ryan M. Young, Yi-Lin Wu, Richard P. Van Duyne, George C. Schatz, and Michael R. Wasielewski*

†Department of Chemistry and Institute for Sustainability and Energy at Northwestern, Northwestern University, Evanston IL 60208-3113

ABSTRACT

Singlet fission (SF) converts a singlet exciton into two triplet excitons in two or more electronically coupled organic chromophores, which may then be used to increase solar cell efficiency. Many known SF chromophores are unsuitable for device applications due to chemical instability or low triplet state energies. The results described here show that efficient SF occurs in derivatives of 9,10-bis(phenylethynyl)anthracene (BPEA), which is a highly robust and tunable chromophore. Fluoro and methoxy substituents at the 4- and 4'-positions of the BPEA phenyl groups control the intermolecular packing in the crystal structure, which alters the interchromophore electronic coupling, while also changing the SF energetics. The lowest excited singlet state (S_1) energy of 4,4′-difluoro-BPEA is higher than that of BPEA, so that the increased thermodynamic favorability of SF results in a $(16 \pm 2\ \text{ps})^{-1}$ SF rate and a 180 ± 16 % triplet yield, which is about an order of magnitude faster than BPEA with a comparable triplet yield. In contrast, 4-fluoro-4′-methoxy-BPEA and 4,4′-dimethoxy-BPEA have slower SF rates, $(90 \pm 20\ \text{ps})^{-1}$ and $(120 \pm 10\ \text{ps})^{-1}$, respectively, and lower triplet yields, 110 ± 4 % and 168 ± 7 %, respectively, than 4,4'-difluoro-BPEA. These differences are attributed to changes in the crystal structure controlling interchromophore electronic coupling as well as SF energetics in these polycrystalline solids.

INTRODUCTION

Singlet fission (SF) is a spin-allowed process involving two or more organic chromophores in which absorption of a photon creates a singlet exciton, which is energetically down-converted into a correlated triplet pair $^1(T_1T_1)$ state, which decorrelates to form two triplet excitons ($T_1 + T_1$).[1] There has been increased research interest in SF because incorporating SF chromophores that absorb blue light into single-junction photovoltaic cells boosts their theoretical power conversion efficiency limit from 34% to 45%, when they are paired with a second chromophore that absorbs red light.[2] Considering this potential device application, significant research is focused on identifying photo-stable SF chromophores that can produce triplet states with sufficiently high energy to generate the requisite electron-hole pairs within a solar cell. Our recent work,[3] and that of Manna et al.[4] show that thin films of polycrystalline 9,10-bis(phenylethynyl)anthracene (BPEA) undergo rapid SF. BPEA has a relatively high first triplet excited state energy, $E(T_1)$ = 1.12-1.30 eV, excellent thermal and photo-stability,[5-7] and versatile synthetic modularity.[7, 8] However, SF in BPEA thin films is complicated by the presence of two polymorphs for which the SF efficiency differs significantly. One polymorph undergoes near quantitative SF, while the other is less than half as efficient. This polymorph dependence is attributed to the difference in lateral slip distance between the BPEA molecules in the solid, where a longer lateral slip distance results in more favorable electronic coupling, facilitating faster and more efficient SF.

The SF rate and efficiency for organic chromophores in the solid state depend on interchomophore electronic coupling, which in turn, depends on the crystal morphology. The role of coupling becomes more critical in cases where SF is either isoergic or somewhat endoergic. For example, perylenediimide (PDI) structures that undergo facile SF have about a 3 Å slippage along the N-N long-axis direction of the PDIs resulting in high SF yields even though the process is

endoergic by about 0.2 eV.[9, 10] In tetracene systems, which are also endoergic by about 0.2 eV, efficient SF is observed when slippage occurs either in the long- or short-axis directions with weaker π-π interactions.[11] Similar behavior is observed for diketopyrrolopyrroles, where SF is isoergic and may be mediated by an excimer state having significant CT character.[12, 13] In contrast, for systems wherein SF is exoergic, such as pentacenes[14-20] and terrylenediimides,[21-25] a wider variety of interchromophore geometries leads to highly efficient SF.

Here we describe a series of BPEA derivatives **1-3** (Scheme 1) to study how substituents on BPEA affect its S_1 and T_1 energies as well as its crystal structure, which tunes their interchromophoric electronic couplings and further modifies their S_1 and T_1 energies by enforcing conformational changes on the substituted BPEA monomers. We find that the S_1 energy of **1** increases slightly compared to BPEA, which results in the fastest SF rate and the highest triplet yield, while the substituent and crystal morphology changes of **3** results in a slightly lower S_1 energy and slower, less efficient SF. The electronic push-pull character in **2** significantly lowers the charge-transfer (CT) state energy resulting in slower SF with a lower yield. The results shown here demonstrate that for similar crystal structures, a greater free energy change results in faster,

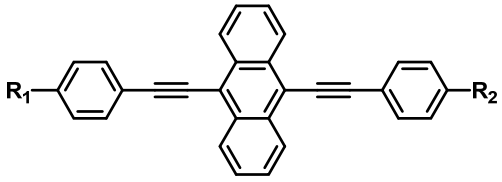

	R_1	R_2
BPEA	H	H
1	F	F
2	F	OMe
3	OMe	OMe

FIG 1. The BPEA derivatives used in this study.

more efficient SF, while CT state participation reduces the SF rate and efficiency in BPEA derivatives.

EXPERIMENTAL AND COMPUTATIONAL METHODS

Synthesis

The synthesis and characterization of **1** and **2** are reported in the Supplementary Material.

Single crystal structure and x-ray spectroscopy

The crystal structure of **3** has been reported previously. Crystals of **1** and **2** were grown by slow solvent evaporation of each compound from chloroform solutions. The crystals were mounted on a polymer loop with Paratone oil, and the data were collected at 100 K on a Bruker Kappa APEX II CCD diffractometer equipped with a Cu Kα 1 μS microfocus source with MX optics. The data were absorption-corrected using SADABS. The structure was solved using SHELXT and refined using SHELXL using Olex 2 software.[26] The structures have been deposited in the Cambridge Crystallographic Data Centre database **1:** CCDC number for **1** is 1909837 and for **2** is 1907242 (Table S1).

Film preparation details

Thin film samples were deposited on sapphire substrates at room temperature at a rate of 0.2 Å/s in a vacuum thermal evaporator (Denton Vacuum DV502-A), followed by solvent-vapor annealing using CH_2Cl_2 overnight. Film thicknesses were measured at 10 different spots with a Veeco Dektak 150 surface profilometer with a 5.0 μm diameter stylus and the average values are 125 ± 10 nm for **1**, 110 ± 4 nm for **2** and 82 ± 7 nm for **3**.

Steady-state spectroscopy

Steady-state absorption spectra of the solution samples were measured using a Shimadzu UV-1800 spectrometer and scatter-corrected spectra of the film samples were measured using a

Shimadzu UV-3600 UV/Vis/NIR spectrometer equipped with an integrating sphere. Steady-state fluorescence spectra of solution and film samples were measured in the front-face mode with a HORIBA Nanolog spectrofluorimeter equipped with an integrating sphere (Horiba Quanta - φ) for absolute fluorescence quantum yield determination.

Triplet energies

Two different triplet sensitizers, palladium octabutoxyphthalocyanine, $PdPc(OBu)_8$[27] and Pd-NDP (Fig. S2),[28] $E(T_1)$ = 1.12 eV and 1.30 eV, respectively, were used to determine the triplet energy of the BPEA derivatives in solution. The synthesis and photophysical properties of $PdPc(OBu)_8$ were reported in previous studies. Fig. S1 shows the steady-state absorption spectrum of Pd-NDP in deoxygenated CH_2Cl_2. The triplet energy of Pd-NDP was determined by measuring its phosphorescence spectrum (Fig. S2) using an HORIBA Nanolog spectrophosphorimeter with an InP/InGaAs detector. A 560 nm pulsed light source was used to obtain the phosphorescence lifetime of Pd-NDP. To determine the triplet spectra of **1-3** in thin films, CH_2Cl_2 solutions containing **1-3** and $PdPc(OBu)_8$ (9:1 weight ratio) at a concentration of 15 mg/mL were spin-coated at 1000 rpm. Fig. S5 shows the steady-state absorption spectra and excited-state dynamics of the sensitized films. In order to confirm triplet formation in the thin films of **1-3** and estimate their triplet energies, oxygen ($E(S_1)$ = 0.98 eV) was also used as a triplet energy acceptor.

Transient absorption spectroscopy

Femtosecond transient absorption spectroscopy (fsTA) experiments at a 1 kHz repetition rate were conducted using a regeneratively amplified Ti:sapphire laser system operating at 828 nm and frequency-doubled to 414 nm as described previously.[29] Solution samples were prepared in a 2 mm path length glass cuvette and degassed with three freeze-pump-thaw cycles. FsTA experiments on the thin films were performed using 14 nJ, 414 nm, 100 fs excitation pulses generated by a 100

kHz repetition rate laser system described in detail previously,[12] but with a few modifications needed to probe 390-490 nm. The 414 nm pump pulse was generated by a non-collinear parametric amplifier (Spirit NOPA 2H, Spectra Physics), which was seeded by 1.25 W from a Spirit amplifier (4 W, 300 fs, Spirit 1040-4, Spectra Physics). Before reaching the sample, the pump was chopped at 50 kHz and was focused to a 1 mm spot size at the sample using a pinhole. The visible–NIR continuum was generated as previously described;[30] however, this study also required a UV-visible continuum probe. This UV-visible continuum was generated using the remaining ~2.75 W of Spirit 1040 nm output focused into a β-barium borate crystal (Type I at 1040 nm, 1.5 mm thick, Eksma Optics) to generate 520 nm pulses, which were then used to drive white light generation. The residual 1040 nm fundamental was removed using a 1000 nm short-pass filter (SPF) before the 520 nm beam was focused into a 5 mm yttrium aluminum garnet (YAG) crystal to generate a continuum from 390 – 580 nm. This continuum was truncated by a 500 nm SPF to remove the residual 520 nm pump light before being focused onto the sample. Detection was carried out with a lab-built spectrometer and 100 kHz CMOS line camera as described previously.[12] The 420-490 nm continuum from this set-up combined with the 490-800 nm continuum generated using 1040 nm allowed probing over a broad spectral range. Nanosecond transient absorption (nsTA) spectroscopy was performed with a 7 ns, 416 nm laser pulse at 10 Hz repetition rate. Details of the apparatus are given elsewhere.[29]

Picosecond time-resolved fluorescence (psTRF) spectroscopy

The output of a non-collinear optical parametric amplifier (Light-Conversion, LLC, Spirit-NOPA) pumped by an amplified Yb:KGW femtosecond laser (Spectra-Physics, Spirit-4) operating at 100 kHz was used for psTRF. The film samples were kept under vacuum inside a cryostat at 295 K and were excited with 420 nm, ~100 fs, 0.6 nJ/ pulses. The TRF signal was collected using

a streak camera system (Hamamatsu C4334 Streakscope) at three different time windows of 1ns, 5ns and 50 ns with instrument response functions of 20 ps, 90 ps, and 1 ns, respectively, to capture the excited state dynamics (Figs. S10-S13).

Data processing and global analysis

The fsTA and psTRF data were subjected to global kinetic analysis to obtain the evolution- and decay-associated spectra respectively, and kinetic parameters as described in detail previously.[23]

Comparison of thermal spectra to fsTA spectra

In order to distinguish the triplet spectrum from the thermally induced spectral shift in the ground-state bleach, the triplet spectra obtained from the fsTA data are compared to the thermal difference ground-state spectrum between high temperature and room temperature in Fig. S8. The steady-state UV-vis spectra at different temperatures were collected using a Shimadzu UV-1800 spectrometer with a temperature controller.

Computational details

The electronic couplings were calculated from the integral matrix elements using the Amsterdam Density Functional (ADF) package[31] at the density functional level of theory (DFT). The triple ζ with two polarization functions (TZ2P) basis set and the B3LYP exchange-correlation functional were chosen. Fock and overlap integral matrix elements were calculated using the TRANSFERINTEGRALS key with the fragment orbital approach as implemented in ADF.

The effective coupling between orbitals *i* and *f*, V_{if}, was calculated using the following equation:[32]

$$V_{if} = \frac{J_{if} - \frac{1}{2}S_{if}(e_i + e_f)}{1 - S_{if}^2} \quad (1)$$

where J_{if} is the Fock matrix element between a pair of monomers, S_{if} is the overlap integral, e_i and e_f are the Fock matrix elements within a monomer. The calculated matrix elements are shown in Table S3.

Singlet and triplet excitation energies, $E(S_1)$ and $E(T_1)$, were calculated using the time-dependent density functional theory (TDDFT) with the ADF package. $E(T_1T_1)$ was obtained by doubling $E(T_1)$. The CT state energy, E(CT), was calculated using a Weller-like equation:

$$E(\mathrm{CT}) = IP + EA + E_{\mathrm{elec}} + E_{\mathrm{ind}} \quad (2)$$

Here, ionization energy (*IP*) and electron affinity (*EA*) of monomer were obtained from DFT, whereas the induction (E_{ind}) and electrostatic (E_{elec}) energies were determined using the classical the Direct Reaction Field (DRF) method[33] suggested by Mirjani *et al*.[34] Atomic charges of both neutral and charged dimers for DRF calculations were obtained from Mulliken population analysis using DFT. The calculated values energies are shown in Table S4.

Considering the first-order coupling of CT states to the initially excited singlet state, S_1, and the final triplet state, (T_1T_1), the effective electronic coupling for the superexchange mechanism,[35] $J_{\mathrm{SE,eff}}$, was calculated using the Eq. 3:

$$\mathrm{J_{SF,eff}} = <\mathrm{S_1S_0^1}|\widehat{\mathrm{V}}|\mathrm{T_1T_1^1}> = <\mathrm{S_1S_0^0}|\widehat{\mathrm{H}}_{\mathrm{el}}|\mathrm{T_1T_1^0}> - \frac{2(\mathrm{V_{LL}V_{LH}} - \mathrm{V_{HH}V_{HL}})}{[\mathrm{E(CT)} - \mathrm{E(TT)}] + [\mathrm{E(CT)} - \mathrm{E(S_1)}]} \quad (3)$$

The first term on the right-hand side of the equation will be ignored since the direct two-electron coupling is small compared to the four 1-electron coupling. V_{LL} and V_{HH} are the 1-electron coupling of the LUMO and HOMO of the two molecules, respectively, whereas V_{LH} and V_{HL} are the electronic couplings between the LUMO of the first molecule and the HOMO of the second molecule, and vice versa. Using the values specified in Table S3 and S4, $J_{\mathrm{SE,eff}}$ values were determined to be 2.8 meV, 8.5 meV, and -3.8 meV for **1**, **2**, and **3** respectively**.**

RESULTS

Structural characterization

The preparation of **1** and **2** is described in detail in the Supplementary Material, while **3** was prepared as described previously.[36] Briefly, commercially available 9,10-dibromoanthracene was subjected to a palladium-catalyzed Sonagashira cross-coupling reaction in the presence of the appropriate phenylacetylene derivatives. Highly crystalline thin films (~100 nm thickness) of the BPEA derivatives were fabricated by thermal vapor deposition on sapphire substrates followed by solvent vapor annealing with CH_2Cl_2 for 12 h. The powder x-ray diffraction (PXRD) patterns of the films are compared to the simulated PXRD patterns in Fig. 1. The single crystal structure of the derivatives was used to simulate the PXRD pattern. We report the crystal structures of **1** and **2** here, while that of **3** has been reported previously.[37] Molecules **1**, **2**, and **3** crystallize into the *C*2/*c*, $P2_1$, and $P2_1/c$ space groups, respectively. Detailed information regarding the single crystal structures are given in the Supplementary Material. The PXRD pattern of the polycrystalline powder scraped off a vapor-deposited/annealed film on sapphire substrates and the grazing incidence x-ray pattern of the film are in good agreement with the simulated PXRD pattern derived from the single crystal data (Fig. 1), indicating that unlike the parent BPEA, there is a single polymorph present in the thin films of **1-3**.

The chromophore packing within the crystal structures of **1-3** is analyzed by extracting the nearest dimer unit within the crystal structure (Fig. 1). From this dimer, the π–π distances and lateral and longitudinal slip distances are calculated. The π–π distance in each derivative is ~3.4 Å (Table 1). Molecule **1** has a large longitudinal slip distance (7.28 Å) but almost no lateral slip, while **2** and **3** have significant lateral slip distances of 3.93 Å and 3.87 Å, respectively, and almost no longitudinal slip. The lateral slip distances in **2** and **3** are similar to those observed in the

polymorphs of BPEA crystals (*C*2/*c* has 4.06 Å and *Pbcn* has 3.33 Å).[3] The longitudinal slip distance of **1** is significantly longer than the 0.80 Å longitudinal slip observed in BPEA, while both **2** and **3** have shorter longitudinal slip distances than BPEA.

Table 1. π–π, lateral and longitudinal slip distances of the nearest dimer unit within the crystal structures of **1-3** and BPEA.

Dimer Unit	π – π (Å)	Lateral slip distance (Å)	Longitudinal slip distance (Å)
1	3.35	0.367	7.280
2	3.41	3.93	0.345
3	3.42	3.87	0.336
BPEA (*C*2/*c*)	3.40	4.06	0.800
BPEA (*Pbcn*)	3.45	3.34	0.800

Photophysical Characterization of BPEA Derivatives

The energy of the lowest singlet excited state, $E(S_1)$, was determined from the crossing points of the steady-state absorbance and emission spectra (Fig. 2) yielding $E(S_1) = 2.65$, 2.59, and 2.59

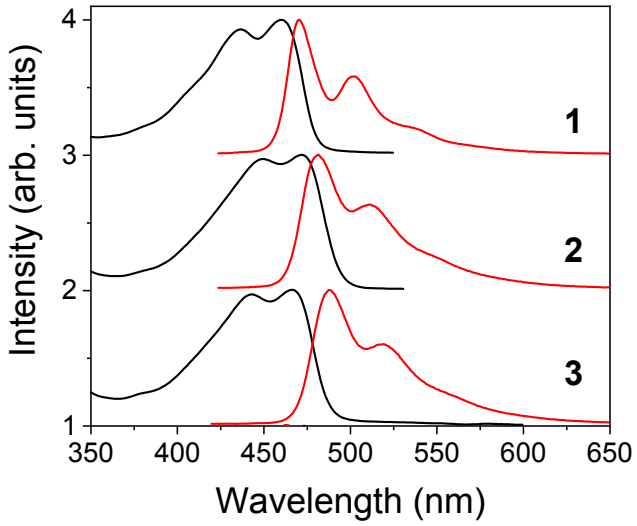

FIG. 2. Steady-state absorbance (black) and emission (red) spectra of the BPEA derivatives in CH_2Cl_2.

eV for **1**, **2**, and **3**, respectively. $E(S_1)$ for **1** is slightly higher in energy than BPEA (2.64 eV), while **2** and **3** are slightly lower. The excited-state dynamics of **1-3** in solution were studied using femtosecond transient absorption (fsTA) spectroscopy, and the spectra and global kinetic analyses are shown in Fig. S3. The S_1 decay rates in solution are $(3.5 \pm 0.2 \text{ ns})^{-1}$, $(3.20 \pm 0.02 \text{ ns})^{-1}$, and $(2.90 \pm 0.03 \text{ ns})^{-1}$ for **1**, **2**, and **3**, respectively, and are similar to that observed for BPEA $(3.17 \pm 0.02 \text{ ns})^{-1}$.[38] The fluorescence quantum yield is 100% for **1** and **2** and 96% for **3**.

The first excited-state triplet energies, $E(T_1)$ of the derivatives in solution were estimated using two triplet sensitizers: palladium octabutoxyphthalocyanine, $PdPc(OBu)_8$[27] and Pd-NDP (Fig. S2),[28] which have $E(T_1)$=1.12 eV and 1.30 eV, respectively. The phosphorescence spectrum of Pd-NDP is shown in Fig. S2. In a mixed solution of each BPEA derivative and the Pd-NDP triplet sensitizer, we selectively excited the sensitizer at 560 nm, which then undergoes intersystem crossing with a $(2.5 \pm 0.2 \text{ ps})^{-1}$ rate, followed by triplet energy transfer to the BPEA derivatives in a few microseconds (Fig. S4). The same experiment was performed with the $PdPc(OBu)_8$ triplet sensitizer resulting in no observed triplet energy transfer to **1-3**. Therefore, the triplet energy range

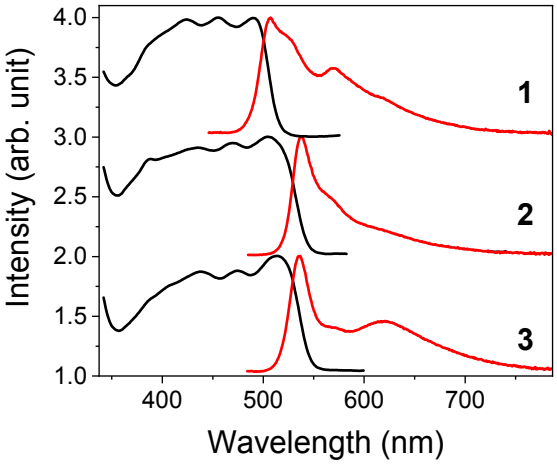

FIG. 3. Steady-state absorbance and emission of thin films of **1-3**.

of **1-3** in solution is $E(T_1)$ =1.12-1.30 eV. The S_1 energy changes significantly in the thin films,

where differences in the crystal structures change the dipole-dipole interactions and orbital overlap between the chromophores, which ultimately alter the electronic structure in the solid state.[39] Compared to $E(S_1)$ = 2.43 eV for BPEA, $E(S_1)$ = 2.48, 2.34, and 2.34 eV for **1**, **2**, and **3**, respectively (Fig. 3). The fluorescence quantum yields are 1.8 ± 0.2 % for **1**, 1.6 ± 0.2 % **2** and 1.8 ± 0.2 % for **3**. Intermolecular coupling between the chromophores lowers $E(S_1)$ by ~200 meV compared to that of the respective monomer. Although the change in S_1 energy among the BPEA derivatives compared to BPEA is small, slight changes in the $S_1 - T_1$ energy gap can lead to significant differences in the SF dynamics.[10]

The triplet sensitization strategy employed in solution to determine the T_1 energies of **1-3** was also used to estimate these energies in the thin films. Thin films of **1-3** containing about 10 weight percent of the $PdPc(OBu)_8$ triplet sensitizer were selectively excited at 680 nm (Fig. S5). FsTA spectra of these films show that the triplet-triplet energy transfer from $PdPc(OBu)_8$ to **1-3** occurs in < 1 ns to yield the respective T_1 states of **1-3**. In separate experiments, excitation of the films of **1-3** at 420 nm in air results in singlet oxygen emission at 1270 nm, indicating energy transfer from the triplet state of **1-3** to triplet oxygen (Fig. S7). These results indicate that 1.12 eV > $E(T_1)$ > 0.98 eV for **1-3** in the thin films.

Excited-state dynamics of BPEA derivative thin films

In order to examine the singlet excited-state deactivation pathways, low-fluence fsTA spectroscopy and picosecond time-resolved fluorescence (psTRF) spectroscopy were used with excitation densities of (1.0×10^{17} excitons·cm^{-3}) and (5.0×10^{15} excitons·cm^{-3}), respectively. It is crucial that the excited-state be studied in the low excitation regime; otherwise, singlet-singlet annihilation can compete with SF and complicate the kinetic analysis, resulting in widely varying apparent SF rates.[4, 24, 29]

From the fsTA spectra, we observe ground-state bleaching (GSB), stimulated emission (SE) and singlet excited-state absorption (ESA) at early times (Fig. 4). The spectra are broadened compared to the singlet ESA observed in solution (Fig. S3). At later times, the spectral changes observed around 450-550 nm indicate the formation of a new state. The feature observed at later times in the fsTA spectra closely resembles the triplet spectra of the BPEA derivatives sensitized with $PdPc(OBu)_8$ (Figs. S5-S6), thus we assign the long-time component in the fsTA spectra to the triplet. In addition to the spectral similarity, triplet formation is further confirmed by observing singlet oxygen emission (Fig. S7). However, one should be cautious in fitting the spectra in the region where the triplet ESA and GSB overlap because thermal distortions of the transient spectra can arise from heating caused by laser excitation.[40, 41] In fact, comparing the fsTA spectra obtained at later times to the thermal difference spectra, which are obtained from the difference between the steady-state absorption spectrum at high temperature and that at room temperature, the spectra are indeed similar, but the relative magnitudes of the signals are quite different (Fig. S8). Although there is undoubtedly some degree of thermal effect observed in the fsTA spectra, its influence on the extracted kinetics was minimized by fitting the data only in the regions where there is no overlap with the GSB.

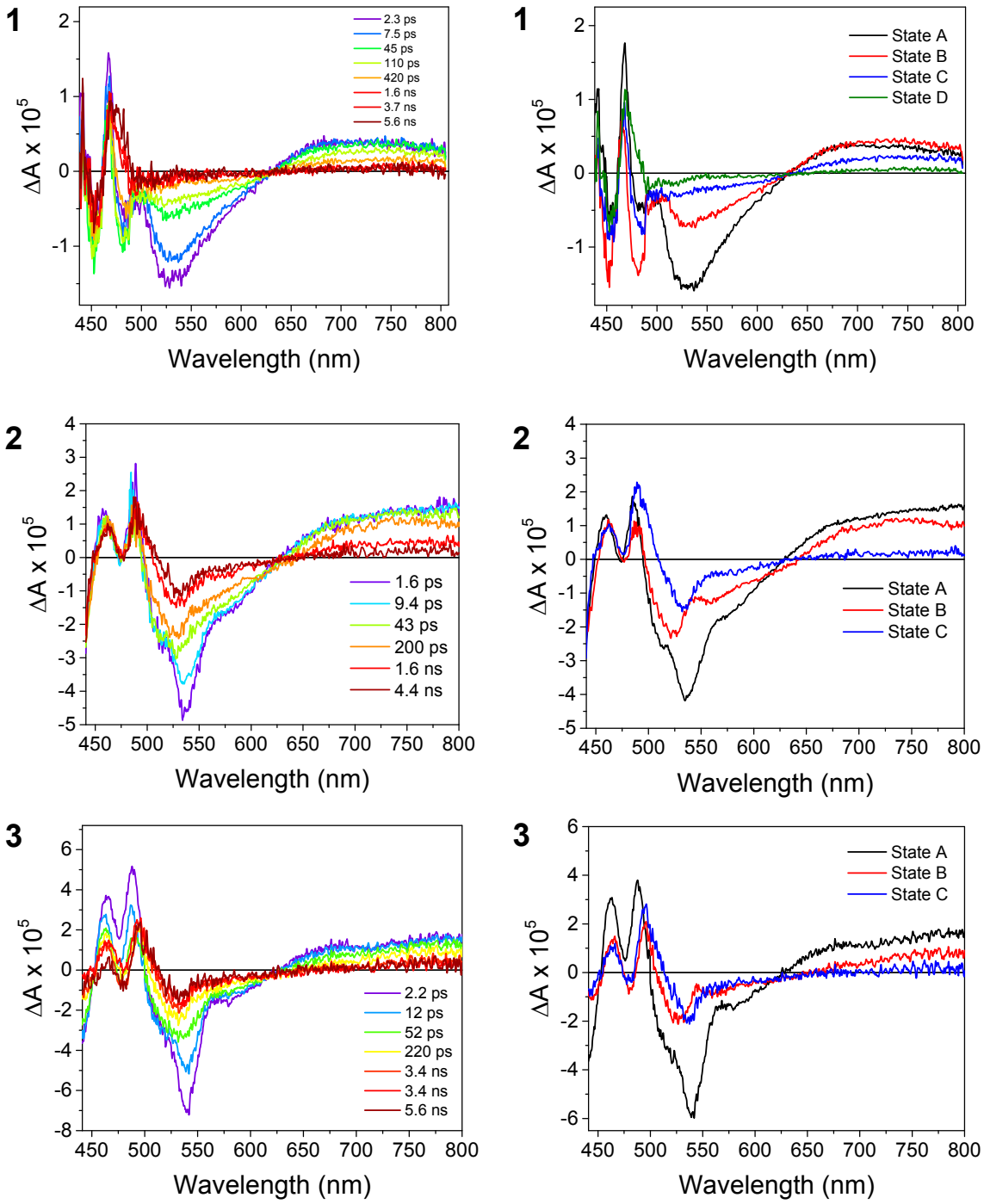

Fig. 4. Left: Low-fluence fsTA spectra at selected time points. Right: evolution-associated spectra from the kinetic fitting using the model discussed in the text. The films are excited at 420 nm (14 nJ/pulse) with the pump spot size of 1mm.

Table 2. Time constants from global fits of the fsTA data to the model described in the text.[a]

Compound	τ_1 (ps)	τ_2 (ns)	τ_3 (ns)	τ_4 (ns)
1	16 ± 2	0.12 ± 0.01	1.2 ± 0.3	>> 7.4
2	90 ± 20	1.1 ± 0.1	>> 7.4	
3	120 ± 10	2.3 ± 0.6	>> 7.4	

[a]Reported values are from the average and standard deviation from multiple experiments.

The initial spectral features arise from S_1 and the later time features are attributed to $^1(T_1T_1)$ and $(T_1 + T_1)$. The fsTA spectra for **1** in Fig. 4 were globally fit using the kinetic model A → B → C → D → ground state (GS), while the spectra for **2** and **3** were fit using A → B → C → ground state (GS). The time constants for each process are given in Table 2 and the kinetic fits and state populations are shown in Fig. S9. Although the evolution-associated spectra shown in Fig. 4 cannot spectrally separate each species completely due to the broadened spectral features and similarity in rate constants, the nature of the intermediate states can be inferred from the degree the spectral changes in the ESA seen by fsTA spectroscopy as well as the psTRF spectra shown below.

We performed psTRF spectroscopy to further examine the excited state dynamics at lower excitation density to minimize singlet-singlet annihilation and interrogate longer times. The data and decay-associated spectra from the first 1 ns are shown in Fig. 5 with additional spectra and kinetic fits shown in Figs. S10-S15. The time constants obtained from the psTRF data (Table 3) are generally in good agreement with those from the low fluence fsTA (Table 2), indicating that fsTA spectra are collected in the near absence of singlet-singlet annihilation.

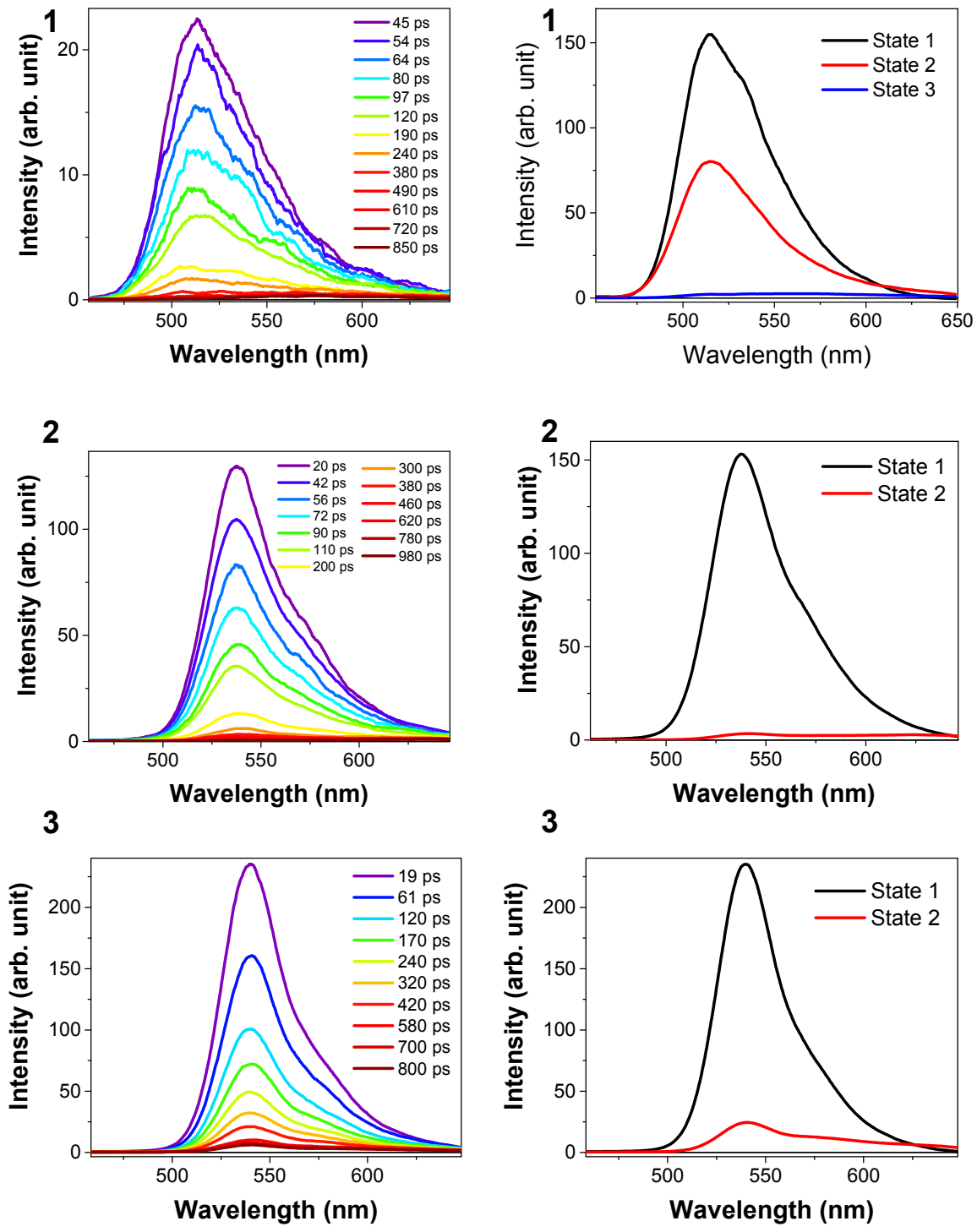

FIG. 5. Left: psTRF spectra at selected time points. Right: decay-associated spectra from the kinetic fitting using the model discussed in the text. The films are excited at 420 nm (0.6 nJ/pulse) with pump spot size of 300 μm.

Table 3. Time constants and amplitudes from psTRF spectroscopy[a]

Compound	τ_1 (ps) (A_1)	τ_2 (ns) (A_2)	τ_3 (ns) (A_3)	τ_4 (ns) (A_4)
1	30 ± 20 (0.65)	0.21 ±0.02 (0.33)	2.0 ± 0.1 (0.02)	8.0 ± 0.5 (<0.01)
2	70 ± 20 (0.98)	1.5 ± 0.1 (0.02)	14 ± 1 (<0.01)	-
3	120 ± 20 (0.90)	2.6 ± 0.8 (0.10)	19 ± 1 (<0.01)	-

[a]Reported values are from the average and standard deviation from multiple experiments.

Triplet yields

The triplet yields (Φ_T) were determined using the singlet depletion method. This method is independent of the choice of kinetic model and is a well-established method in quantifying triplet yields for systems with overlapping triplet ESA and GSB signals, such as rylene diimides,[24, 29] diketopyrrolopyrroles,[12, 13] and polyacenes.[3, 11, 29] The singlet depletion method approximates the number of triplet excitons created per singlet exciton by quantifying the ground-state bleach spectrum resulting from the triplet excited-state population. First, the ground-state bleach is estimated from the excitation energy, wavelength, and spot size, as well as the film density from the thickness and crystal structure (Table S2). Detailed information regarding the triplet yield calculations is given in the Supplementary Material. Data was collected from two different spots on each film and both datasets give similar results. First, the triplet yield is obtained at 50 ns where the only transient signals arise from the triplet state, and then extrapolated back to 1 ns, which is at least five times longer than the longest S_1 decay component of **1-3** as determined from the psTRF data, to correct for population loss occurring after the SF event. In addition to the absolute triplet yield, the triplet yields relative to that of **1** are reported to accommodate complication in the triplet yield calculation used due to the thermal effect. The data are shown in Table 4.

Table 4. Triplet yields and triplet decay time constants and amplitudes.

Film	Φ_T at 50 ns	Φ_T at 1 ns	Relative Φ_T	τ_1 (ns) (A_1)	τ_2 (μs) (A_2)
1	90 ± 10 %	180 ± 16 %	1	74 ± 10 (0.97)	4.5 ± 2.0 (0.03)
2	50 ± 5 %	110 ± 4 %	0.61	82 ± 8 (0.90)	>> 4 μs (0.10)
3	44 ± 6 %	168 ± 7 %	0.93	29 ± 8 (0.92)	0.43 ± 0.06 (0.08)

[a]Reported values are from the average and standard deviation from multiple experiments.

DISCUSSION

The significant decrease in fluorescence quantum yields and the singlet excited-state lifetimes in the thin films of BPEA derivatives compared to the solutions indicate that there are additional photophysical decay pathways in the crystalline solid state. In the case of **1**, the psTRF spectra shown in Fig. 5 reveal two spectral components with τ_1 and τ_2 that closely resemble the steady-state emission spectra of **1-3**, while the third, very minor spectral component with τ_3 is red-shifted to 564 nm (2.20 eV) (Fig. S14). This indicates that both τ_1 and τ_2 involve S_1 decay, while τ_3 most likely results from a small population of the excimer state that decays with τ_3 = 2.0 ns. Although there is a single polymorph in the thin film of **1**, if some degree of heterogeneity exists in terms of grain size and crystallinity, such heterogeneity could lead to formation of local hot spots where SF is more favorable, as seen in pentacene[42] and terrylenediimide films.[24] Comparing the ratio of the S_1 populations A and B in the decay-associated psTRF spectra at 515 nm (Fig. 5), 65% of the triplets come from A and 33% from B.

The evolution-associated fsTA spectrum A for **1** shows an immediate GSB at 450 and 480 nm as well as a broad SE feature at 525 nm, and an ESA at 625-800 nm. The corresponding spectrum B shows a substantial decrease in the SE feature and growth of the bleach at 450 and 480 nm, while the ESA at 625-800 nm remains nearly constant. This is consistent with the formation of the $^1(T_1T_1)$ state of **1**, as GSB growth has been observed for other chromophores undergoing SF.[43] The degree

of GSB growth often depends on the degree of spectral overlap between the GSB and the transient absorption spectrum of $^1(T_1T_1)$. Spectrum C shows significant loss of the SE feature and the ESA, while the GSB remains, and spectrum D leaves essentially only the GSB. The final triplet spectrum at long times is consistent with decorrelation of the $^1(T_1T_1)$ state resulting in long-lived triplets (T_1 + T_1). The long-lived absorption features in spectra C and D closely match the triplet-sensitized TA spectra of **1-3** (Fig. S6).

The psTRF spectra for **2** shown in Fig. 5 are dominated by a single S_1 decay component along with a very weak excimer emission component with a maximum at 623 nm (1.99 eV) (Fig. S14). The electronic push-pull character of the methoxy and fluoro groups in **2** result in an excimer state with more CT character than that of **1**, resulting in a more red-shifted excimer emission band that decays with τ_3 = 12 ns. The evolution-associated fsTA spectra of **2** (Fig. 4) show similar characteristics to those of **1**, except that only three kinetic components are found. This is consistent with the single S_1 decay component observed by psTRF. FsTA spectrum A once again shows significant SE at 530 nm and ESA at 625-800 nm. However, the GSB features are dominated by the overlying ESA between 450 and 480 nm. This spectrum evolves to give spectrum B that shows significant loss of SE, slight loss of ESA at 625-800 nm, and much less loss at the 460 and 490 nm ESA. The band at 490 nm continues to grow with the corresponding loss of the SE and NIR ESA features. Once again, the triplet features at 450-500 nm persist at longer times after the S_1 spectral features have decayed. Moreover, since the psTRF data show only one significant S_1 decay component, fsTA spectra B and C most likely result from the $^1(T_1T_1)$ and (T_1 + T_1) states, respectively.

Among the three derivatives, molecule **2** has the lowest SF yield. Presumably, having push-pull character in **2** lowers its CT state energy. The energy of the CT states of **1-3** were calculated

using a combination of density functional theory (DFT) and molecular mechanics (MM).[44] The computed CT state energies are 3.42 eV (**1**), 3.24 eV (**2**), and 3.5 eV (**3**). Since these computations do not take into account the dielectric environment in the crystal, one should only consider the relative CT state energies. These energies show that the CT state energy of **2** is about 0.2 eV lower than that of **1** and **3.** Although strong push-pull character in some copolymers is known to facilitate SF by lowering the CT state energy,[45] the low CT energy in **2** may hinder SF. This apparent contradiction can be explained in terms of the superexchange mechanism of SF.[35] As the energy of the virtual CT state decreases, the SF rate should increase, but only until the CT state energy is nearly isoenergetic to or below that of the S_1 and $^1(T_1T_1)$ states. At that point, state mixing becomes significant or in the limit the CT state becomes a real intermediate and can act as a trap state impeding SF. A similar phenomenon has been observed in terrylenediimide dimers.[25]

Finally, molecule **3** displays psTRF spectra similar to those of **2** (Fig. 5) except that a second S_1 emission component (τ_2) now constitutes about 10% of the amplitude of the dominant S_1 component (τ_1). The evolution-associated fsTA spectra of **3** (Fig. 4) show similar characteristics to those of **2**, except that the data analysis does not reveal a second spectrum that corresponds to the second minor S_1 decay component observed by psTRF. Evolution-associated fsTA spectrum A is again attributed primarily to decay of the initial S_1 state followed by the formation of two states that are primarily triplet in character. As in **1**, these two similar spectra, B and C, may result from the $^1(T_1T_1)$ and $(T_1 + T_1)$ state contributions, respectively.

As noted above, the differences in the crystal structures of **1-3** ultimately affect the interchomophore electronic coupling in the excited state. For example, **1-3** have similar π-π distances (~ 3.40 Å) with **1** having the largest long-axis slip distance, which originates from an increase in the dihedral angle between the anthracene core and the phenyl (Fig. 1). The large

dihedral angle decreases the electronic conjugation between the anthracene core and phenyl group, which leads to a higher S_1 energy and elongation of the long-axis slip due to increased steric hindrance between neighboring molecules in the solid state. The interchromophore electronic couplings of **1-3** were calculated using methods described previously.[3, 44] Among the three derivatives, **1** exhibits the smallest effective electronic coupling (2.85 meV) compared to **2** (8.54 meV) and **3** (-3.80 meV). Given that the observed SF rates do not correlate with these computed couplings, it is clear that the SF rates are also modulated by the electronic structures of the chromophores themselves that result in changes to the S_1 - T_1 energy gaps. Part of this energy gap modulation may result from conformational changes enforced by the crystal structures, similar to that observed in 1,3-diphenylisobenzofuran films.[46] This contrasts with unsubstituted BPEA, where its two different polymorphs have the same S_1 and T_1 energies, such that electronic coupling calculations using the superexhange mechanism predict the relative SF rate ratio reasonably well.[3]

CONCLUSIONS

Molecule **1** has a comparable SF efficiency (Φ_T = 180 ± 16 %) to unsubstituted BPEA. Since the majority of singlet excitons undergo seven-fold faster SF in **1** than in the *C*2/c polymorph in BPEA, this derivative is the most favorable SF chromophore among the BPEA systems explored to date. Both **2** and **3** have lower SF efficiencies and slower SF rates than **1**, which is expected based on previous work,[3] considering that both have shorter lateral slip distances than the *C*2*/c* polymorph of BPEA. The large dihedral angle between the anthracene core and the phenyl substituent in the crystal structure of **1** slightly increases $E(S_1)$, whereas the chromophore interactions in the crystalline **2** and **3** derivatives slightly lower $E(S_1)$. The increase in S_1 energy allows near unity SF efficiency (180 ± 16 %) from the S_1 state in **1**. Both a fast and a slow SF rate are observed, which is attributed to heterogeneity in the film. The decrease in $E(S_1)$ for **2** and **3**

results in slower SF compared to **1**. The lower CT state energy of **2** may also impede SF by providing a trap state. In substituted BPEA systems, the free energy change for SF appears to be the most important factor dictating SF efficiency based on the results shown here. Tailoring the crystal structure to maximize the S_1 energy in BPEA systems along with maintaining a high CT state energy should discourage participation of this state and further enhance SF.

ACKNOWLEDGMENT

This work was supported by the U.S. Department of Energy, Office of Science, Office of Basic Energy Sciences under Award DE-FG02-99ER14999 (M.R.W.). We thank Halina Zhylitskaya and Marcin Stępień for providing a sample of the Pd-NDP photosensitizer. G.K., R.P.V.D., and G.C.S. acknowledge support from the Air Force Office of Scientific Research MURI (FA9550-14-1-0003). GK and GCS (theory work) acknowledge the LEAP Center, DOE grant DE-SC0001059. We thank Dr. Stephen Miller of the Northwestern University Laser and Electronics Design facility for instrumental assistance. This work made use of the IMSERC at Northwestern University, which has received support from the Soft and Hybrid Nanotechnology Experimental (SHyNE) Resource (NSF ECCS-1542205), the State of Illinois, and the International Institute for Nanotechnology (IIN). X-ray crystallography and PXRD was performed at the Jerome B.Cohen X-Ray Diffraction Facility supported by the MRSEC program of the National Science Foundation (DMR-1720139) at the Materials Research Center of Northwestern University and the Soft and Hybrid Nanotechnology Experimental (SHyNE) Resource (NSF ECCS-1542205.) Y.B. thanks Charlotte Stern for helpful discussions regarding X-ray work. Profilometry was performed at the EPIC facility of Northwestern University's NU*ANCE* Center, which has received support from the Soft and Hybrid Nanotechnology Experimental (SHyNE) Resource (NSF ECCS-1542205); the

MRSEC program (NSF DMR-1720139) at the Materials Research Center; the International Institute for Nanotechnology (IIN); the Keck Foundation; and the State of Illinois, through the IIN.

SUPPLEMENTARY MATERIAL

See Supplementary Material for synthesis and characterization of **1** and **2**, single crystal structures and x-ray spectroscopy, additional steady-state and transient spectroscopy details, kinetic analyses, and triplet yield calculations.

REFERENCES

[1] M. B. Smith, and J. Michl, Annu. Rev. Phys. Chem. **64**, 361 (2013).

[2] M. C. Hanna, and A. J. Nozik, J. Appl. Phys. **100**, 074510/1 (2006).

[3] Y. J. Bae, G. Kang, C. D. Malliakas, J. N. Nelson, J. Zhou, R. M. Young, Y. L. Wu, R. P. Van Duyne, G. C. Schatz, and M. R. Wasielewski, J. Am. Chem. Soc. **140**, 15140 (2018).

[4] B. Manna, A. Nandi, and R. Ghosh, J. Phys. Chem. C **122**, 21047 (2018).

[5] W. Fudickar, and T. Linker, J. Am. Chem. Soc. **134**, 15071 (2012).

[6] J. C. Ribierre, A. Ruseckas, H. Cavaye, H. S. Barcena, P. L. Burn, and I. D. W. Samuel, J. Phys. Chem. A **115**, 7401 (2011).

[7] R. Giménez, M. Piñol, and J. L. Serrano, Chem. Mater. **16**, 1377 (2004).

[8] C. V. Suneesh, M. V. Vinayak, and K. R. Gopidas, J. Phys. Chem. C **114**, 18735 (2010).

[9] J. Vura-Weis, M. A. Ratner, and M. R. Wasielewski, J. Am. Chem. Soc. **132**, 1738 (2010).

[10] A. K. Le, J. A. Bender, D. H. Arias, D. E. Cotton, J. C. Johnson, and S. T. Roberts, J. Am. Chem. Soc. **140**, 814 (2018).

[11] E. A. Margulies, N. Kerisit, P. Gawel, C. M. Mauck, L. Ma, C. E. Miller, R. M. Young, N. Trapp, Y.-L. Wu, F. Diederich, and M. R. Wasielewski, J. Phys. Chem. C **121**, 21262 (2017).

[12] C. M. Mauck, P. E. Hartnett, E. A. Margulies, L. Ma, C. E. Miller, G. C. Schatz, T. J. Marks, and M. R. Wasielewski, J. Am. Chem. Soc. **138**, 11749 (2016).

[13] P. E. Hartnett, E. A. Margulies, C. M. Mauck, S. A. Miller, Y. Wu, Y.-L. Wu, T. J. Marks, and M. R. Wasielewski, J. Phys. Chem. B **120**, 1357 (2016).

[14] B. S. Basel, J. Zirzlmeier, C. Hetzer, S. R. Reddy, B. T. Phelan, M. D. Krzyaniak, M. K. Volland, P. B. Coto, R. M. Young, T. Clark, M. Thoss, R. R. Tykwinski, M. R. Wasielewski, and D. M. Guldi, Chem **4**, 1092 (2018).

[15] E. Kumarasamy, S. N. Sanders, M. J. Y. Tayebjee, A. Asadpoordarvish, T. J. H. Hele, E. G. Fuemmeler, A. B. Pun, L. M. Yablon, J. Z. Low, D. W. Paley, J. C. Dean, B. Choi, G. D. Scholes, M. L. Steigerwald, N. Ananth, D. R. McCamey, M. Y. Sfeir, and L. M. Campos, J. Am. Chem. Soc. **139**, 12488 (2017).

[16] B. S. Basel, J. Zirzlmeier, C. Hetzer, B. T. Phelan, M. D. Krzyaniak, S. R. Reddy, P. B. Coto, N. E. Horwitz, R. M. Young, F. J. White, F. Hampel, T. Clark, M. Thoss, R. R. Tykwinski, M. R. Wasielewski, and D. M. Guldi, Nat. Commun. **8**, 15171 (2017).

[17] S. Lukman, K. Chen, J. M. Hodgkiss, D. H. P. Turban, N. D. M. Hine, S. Dong, J. Wu, N. C. Greenham, and A. J. Musser, Nat. Commun. **7**, 13622 (2016).

[18] J. Zirzlmeier, D. Lehnherr, P. B. Coto, E. T. Chernick, R. Casillas, B. S. Basel, M. Thoss, R. R. Tykwinski, and D. M. Guldi, Proc. Natl. Acad. Sci. USA **112**, 5325 (2015).

[19] M. J. Y. Tayebjee, K. N. Schwarz, R. W. MacQueen, M. Dvorak, A. W. C. Lam, K. P. Ghiggino, D. R. McCamey, T. W. Schmidt, and G. J. Conibeer, J. Phys. Chem. C **120**, 157 (2016).

[20] Y. Wu, K. Liu, H. Liu, Y. Zhang, H. Zhang, J. Yao, and H. Fu, J. Phys. Chem. Lett. **5**, 3451 (2014).

[21] M. Chen, M. D. Krzyaniak, J. N. Nelson, Y. J. Bae, S. M. Harvey, R. D. Schaller, R. M. Young, and M. R. Wasielewski, Proc. Natl. Acad. Sci. U. S. A. **116**, 8178 (2019).

[22] A. Mandal, M. Chen, E. D. Foszcz, J. D. Schultz, N. M. Kearns, R. M. Young, M. T. Zanni, and M. R. Wasielewski, J. Am. Chem. Soc. **140**, 17907 (2018).

[23] M. Chen, Y. J. Bae, C. M. Mauck, A. Mandal, R. M. Young, and M. R. Wasielewski, J. Am. Chem. Soc. **140**, 9184 (2018).

[24] E. A. Margulies, J. L. Logsdon, C. E. Miller, L. Ma, E. Simonoff, R. M. Young, G. C. Schatz, and M. R. Wasielewski, J. Am. Chem. Soc. **139**, 663 (2017).

[25] E. A. Margulies, C. E. Miller, Y. Wu, L. Ma, G. C. Schatz, R. M. Young, and M. R. Wasielewski, Nature Chem. **8**, 1120 (2016).

[26] O. V. Dolomanov, L. J. Bourhis, R. J. Gildea, J. A. K. Howard, and H. Puschmann, J. Appl. Crystallogr. **42**, 339 (2009).

[27] B. D. Rihter, M. E. Kenney, W. E. Ford, and M. A. J. Rodgers, J. Am. Chem. Soc. **112**, 8064 (1990).

[28] H. Zhylitskaya, J. Cybińska, P. Chmielewski, T. Lis, and M. Stępień, J. Am. Chem. Soc. **138**, 11390 (2016).

[29] S. W. Eaton, L. E. Shoer, S. D. Karlen, S. M. Dyar, E. A. Margulies, B. S. Veldkamp, C. Ramanan, D. A. Hartzler, S. Savikhin, T. J. Marks, and M. R. Wasielewski, J. Am. Chem. Soc. **135**, 14701 (2013).

[30] R. M. Young, A. P. N. Singh, A. Thazhathveetil, V. Y. Cho, Y. Zhang, N. Renaud, F. C. Grozema, D. N. Beratan, M. A. Ratner, G. C. Schatz, Y. A. Berlin, F. D. Lewis, and M. R. Wasielewski, J. Am. Chem. Soc. **137**, 5113 (2015).

[31] G. te Velde, F. M. Bickelhaupt, E. J. Baerends, C. Fonseca Guerra, S. J. A. van Gisbergen, J. G. Snijders, and T. Ziegler, J. Comp. Chem. **22**, 931 (2001).

[32] N. Renaud, P. A. Sherratt, and M. A. Ratner, J. Phys. Chem. Lett. **4**, 1065 (2013).

[33] M. Swart, and P. T. van Duijnen, Molec. Simul. **32**, 471 (2006).

[34] F. Mirjani, N. Renaud, N. Gorczak, and F. C. Grozema, J. Phys. Chem. C **118**, 14192 (2014).

[35] T. C. Berkelbach, M. S. Hybertsen, and D. R. Reichman, J. Chem. Phys. **138**, 114103 (2013).

[36] R. Göstl, and R. P. Sijbesma, Chem. Sci. **7**, 370 (2016).

[37] W. Clegg, and A. J. Scott, CSD Communication, CCDC 234275 (2017).

[38] A. Demeter, J. Phys. Chem. A **118**, 9985 (2014).

[39] N. J. Hestand, and F. C. Spano, Acc. Chem. Res. **50**, 341 (2017).

[40] A. Rao, M. W. B. Wilson, S. Albert-Seifried, R. Di Pietro, and R. H. Friend, Phys. Rev. B **84**, 195411 (2011).

[41] V. M. Nichols, K. Broch, F. Schreiber, and C. J. Bardeen, J. Phys. Chem. C **119**, 12856 (2015).

[42] K. Broch, J. Dieterle, F. Branchi, N. J. Hestand, Y. Olivier, H. Tamura, C. Cruz, V. M. Nichols, A. Hinderhofer, D. Beljonne, F. C. Spano, G. Cerullo, C. J. Bardeen, and F. Schreiber, Nat. Commun. **9**, 954 (2018).

[43] J. C. Johnson, A. J. Nozik, and J. Michl, J. Am. Chem. Soc. **132**, 16302 (2010).

[44] C. E. Miller, M. R. Wasielewski, and G. C. Schatz, J. Phys. Chem. C **121**, 10345 (2017).

[45] E. Busby, J. Xia, Q. Wu, J. Z. Low, R. Song, J. R. Miller, X. Y. Zhu, L. M. Campos, and M. Y. Sfeir, Nat. Mater. **14**, 426 (2015).

[46] E. A. Buchanan, J. Kaleta, J. Wen, S. H. Lapidus, I. Císařová, Z. Havlas, J. C. Johnson, and J. Michl, J. Phys. Chem. Lett. **10**, 1947 (2019).